Astron. Astrophys. 349, 839–850 (1999)

ASTRONOMY AND ASTROPHYSICS

Multidimensional self-consistent radiative transfer simulations based on the Monte-Carlo method

S. Wolf[1], **Th. Henning**[2], **and B. Stecklum**[1]

[1] Thüringer Landessternwarte Tautenburg, Sternwarte 5, D-07778 Tautenburg, Germany
[2] Astrophysikalisches Institut und Universitäts-Sternwarte (AIU), Schillergässchen 3, D-07745 Jena, Germany

Received 6 April 1999 / Accepted 23 April 1999

Abstract. We developed the first Monte-Carlo code for three-dimensional self-consistent continuum radiative transfer calculations. The density structure of the dust configuration (disk/envelope/molecular cloud core) can be chosen arbitrarily as well as the number, configuration, and radiation parameters of the stars inside this configuration. Binaries and multiple stellar systems (with or without disks around the stars) surrounded by a dusty environment represent typical applications for this code. Apart from the dust temperature, intensity and emergent spectral energy distribution, the polarization of light can be calculated. These polarization maps provide additional information about the geometrical structure and chemical composition of dusty media.

As the first application of our code, we simulated the radiative transfer in a protostellar disk around a star ($M = 1.14\,M_{\odot}$) and a fragmented molecular cloud core. The dust density and temperature distributions have been taken from hydrodynamical simulations.

Key words: polarization – radiative transfer – scattering – stars: circumstellar matter – ISM: clouds – ISM: dust, extinction

1. Introduction

For the interpretation of spectra, images, and polarization maps of young stellar objects (YSO), embedded in molecular clouds, radiative transfer simulations provide the necessary basis. In the past, many methods for the solution of the radiative transfer problem have been developed. While the circumstellar matter as well as molecular and diffuse HI clouds obviously show a fractal and, therefore, a very complex structure (see, e.g., Colomb et al. 1980, Rosen & Bregman 1995, Macchetto et al. 1994, Capetti et al. 1995a,b,c), the models contain often considerable simplifications. The most simple models consist of a point-like star in the centre of an homogeneous spherical envelope with only a radial dust density profile following a power law (see, e.g., Leung 1975, Yorke 1980, Henning 1985, Chini et al. 1986). Because of the conservation of angular momentum and/or the influence of magnetic fields, dust configurations around YSOs, evolved stars, and active galactic nuclei (AGN) are characterized by axial symmetry. Therefore, the effect of different viewing angles can only be simulated with two-dimensional models (see, e.g., Bouquet et al. 1990; Dent 1988, Lopez et al. 1995, Sonnhalter et al. 1995, Menshchikov & Henning 1997: YSOs; Efstathiou & Rowan-Robinson 1990: late-type stars; Spagna et al. 1991: disk-shaped interstellar dust clouds; Pier & Krolik 1992, Stenholm 1994, Efstathiou & Rowan-Robinson 1995, Manske et al. 1998, Manske & Henning 1998: AGNi). However, these models are not able to treat radiative transfer in inhomogeneous structures. In addition, the investigation of systems containing an arbitrary constellation of stars requires three-dimensional radiative transfer codes (e.g., close binary stars with randomly distributed accretion disks). 3D continuum radiative transfer simulations have been performed by Witt & Gordon (1996) and Wolf et al. (1998) (see also, Pagani 1998, Kishimoto 1996, Spaans 1996, Dittmann 1995, Boissé 1990, Boss & Yorke 1990).

In this paper, we present the first *self-consistent* 3D continuum radiative transfer simulation code. "Self-consistency" means here that the dust temperature and therefore the intensity of dust radiation results from the stellar heating and/or other heating processes (heating by dust re-emission, viscous heating in accretion discs). We applied the Monte-Carlo (MC) method because it provides a straightforward solution of the radiative transfer problem even in the case of very complex geometries (see, e.g., Och et al. 1998, Pagani 1998, Lorenz-Martins & De Araujo 1998, Bianchi et al. 1996, Fischer et al. 1994, Whitney & Hartmann 1992, 1993). Our simulations do not require simplifying assumptions: the number, configuration, radiative characteristics (spectral energy distribution, (an)isotropy), and a realistic extent of the heating sources can be choosen arbitrarily as well as the density distribution and the optical behaviour of the scattering particles (electrons, dust grains). Because the random error of the results is approximately inversely proportional to the square root of the number of simulated photons, MC simulations are always very time-consuming. While this was a handicap in the past, nowadays the importance of MC simulations increases because of the increase in computer power and the great advantages of this method described beforehand.

In Sect. 2 we describe the code, in particular the derivation of the spectral energy distribution of the dust (see Sect. 2.2). It follows an overview about tests of the program for different

Send offprint requests to: S. Wolf (wolf@tls-tautenburg.de)

model geometries (see Sect. 3). The results of the first applications of our code are discussed in Sect. 4: the radiative transfer in a protostellar disk and in a fragmented molecular cloud core. In both cases, the spatial density and temperature structure of the configurations were calculated with hydrodynamical simulations (Yorke 1999, priv. communication; Yorke et al. 1993; Boss 1998). Finally, we give an outlook on further applications of our code in Sect. 5.

2. Computational method

2.1. Radiative transfer scheme

The spatial distribution of the stars and the scattering/absorbing medium (dust grains and/or electrons) is defined inside a convex model space. In respect to the radiative transfer, the shape of the model space should be adapted to the symmetry of the configuration (see Appendix A: and Sect. 3).

The radiation energy is partitioned into so-called weighted photons (particle picture). The energy, intensity, and polarization of a weighted photon are described by its wavelength $\lambda_{\rm P}$ and the Stokes vector $(I,Q,U,V)_{\rm T}$. The radiative transfer for each of these photons is subdivided into 3 steps: the emission of a weighted photon by the star or a dust grain, its interaction with dust grains or electrons in the stellar environment, and its observation after leaving the model configuration.

1. *Emission from a star or a dust grain*:
   The initial Stokes vector of each newly emitted unpolarized photon is

$$W \begin{pmatrix} I \\ Q \\ U \\ V \end{pmatrix}_0 = \begin{pmatrix} 1 \\ 0 \\ 0 \\ 0 \end{pmatrix}, \tag{1}$$

   where W symbolizes the relative weight of the photon. The value of W depends on the intensity of emission and is therefore a function of the spatial coordinate of emission and the wavelength λ.
   If we assume isotropic emission (from the star or a spherical dust grain), the directions of emission of all photons are uniformly distributed over $4\pi{\rm ster}$. The angle θ between the direction of propagation and the z-axis of the global coordinate system of the dust configuration is then defined by

$$\cos\theta = -1 + 2\zeta \tag{2}$$

   where ζ is a random number uniformly distributed on the interval $[0,1]$. The corresponding azimuthal angle ϕ is uniformly distributed in the interval $[0,2\pi]$:

$$\phi = 2\,\pi\,\zeta. \tag{3}$$

   For the determination of random numbers, we use a random number generator (RAN2) developed by Knuth (1989). This congruence-generator combines several random number generators to minimize sequential correlations between the random numbers.

2. *Scattering and Absorption*:
   The free path length l of the test photon can be derived from the optical depth $\tau_{\rm ext}$ along l:

$$\tau_{\rm ext} = -\ln(1-\zeta). \tag{4}$$

   The corresponding value of l can be determined by going along the actual direction of test photon propagation $\boldsymbol{R}$ and calculating the sum:

$$\tilde{\tau}_{\rm ext} = \sum_{i=1}^{i_{\rm end}} n(\boldsymbol{R}_{\rm li})\, C_{\rm ext}(\boldsymbol{R}_{\rm li})\, \Delta l_i, \quad l = \sum_{i=1}^{i_{\rm end}} \Delta l_i, \tag{5}$$

   until

$$\epsilon_\tau = \frac{|\tau_{\rm ext} - \tilde{\tau}_{\rm ext}|}{\tau_{\rm ext}} \tag{6}$$

   becomes sufficiently small (we use $\epsilon_\tau = 10^{-3\ldots-5}$). On the one hand, the value of Δl_i has to be small enough to resolve the smallest density structures (see also Sect. 2.3). On the other hand, the calculation of the sum in Eq. 5 is one of the most time-consuming parts of the code. Therefore, we have to find a compromise between these two contrary conditions.
   The modification of the Stokes vector due to the ith interaction can be described with the help of a special 4×4 Mueller matrix $\hat{S}(\theta)$, where θ is the scattering angle (see Appendix B:; see also Bickel & Bailey 1985, Bohren & Huffman 1983).

$$\begin{pmatrix} I \\ Q \\ U \\ V \end{pmatrix}_i \propto \hat{S}(\theta) \begin{pmatrix} I \\ Q \\ U \\ V \end{pmatrix}_{i-1} \tag{7}$$

   In the case of dust scattering this leads to absorption - the weighted photon looses energy but will not vanish. The absorption of energy leads to dust heating. To obtain a spatially resolved dust temperature distribution, the model space is subdivided into smaller volumes, we call *energy storage cells* (ESC). The temperature in a particular cell which is needed for the determination of the SED (spectral energy distribution) of radiation being re-emitted by the dust in the case of passive heating is determined by the amount of absorbed energy in it assuming local thermal equilibrium (LTE). In the case of viscous heating, the corresponding amount of energy has to be added to the absorbed energy in each cell (see Sect. 2.2).
   The new direction of the scattered photon path is determined by the scattering probability distribution function.
3. *Observation*:
   If the photon leaves the model space, it will be "observed" by array-detector-like planes being arranged around the model space (see Fig. 1). The Stokes vector has to be projected onto the respective plane.

For a more detailed description of the solution of the radiative transfer problem in our code, we refer to Fischer et al. (1994).

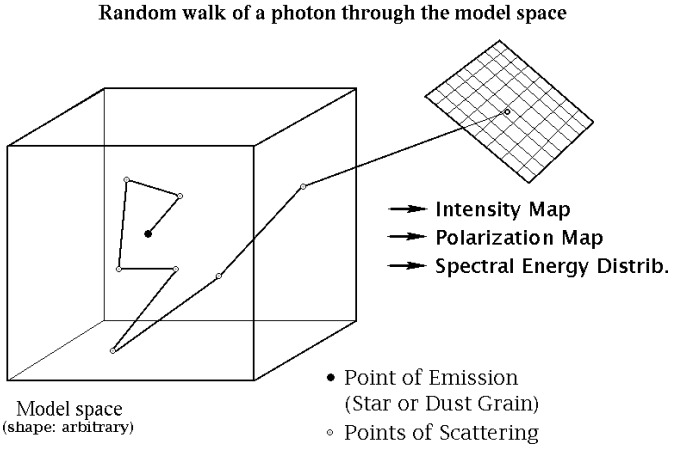

Fig. 1. Random walk of a photon through the model space

2.2. Dust re-emission

Based on the radiative transfer scheme outlined in Sect. 2.1, we now describe the determination of the dust temperatur distribution in the case of passive heating.

Assuming that the star with the radius R_* shows emission of a black body with the temperatur $T_{\rm eff}$ (not a necessary condition for the code), its emitted monochromatic luminosity at the wavelength λ is determined by

$$L^{\rm e}_{\lambda,{\rm Star}} = \pi R_*^2 4\pi B_\lambda(T_{\rm eff}) \tag{8}$$

Due to absorption of the stellar or re-emitted dust radiation, the dust will be heated. The re-emitted monochromatic luminosity of a dust grain with the radius $a_{\rm Grain}$, the temperature $T_{\rm Grain}$, and the wavelength-dependend absorption effiency factor $Q^{\rm abs}(\lambda)$ is given by

$$L^{\rm e}_{\lambda,{\rm Grain}} = \pi a^2_{\rm Grain} 4\pi Q^{\rm abs}(\lambda, a_{\rm Grain}) B_\lambda(T_{\rm Grain}) \tag{9}$$

The conservation of energy of all radiation being absorbed/emitted in/from a cell of volume V leads to the relation

$$N_{\rm V} \int d\lambda L^{\rm e}_{\lambda,{\rm Grain}} = \int d\lambda L^{\rm abs}_{\lambda,{\rm V}}, \tag{10}$$

where $N_{\rm V}$ is the number of dust grains in that volume and $L^{\rm abs}_{\lambda,{\rm V}}$ is the absorbed monochromatic luminosity. Combining Eq. 9 and 10, the (mean) dust grain temperature in the considered volume element can be derived from

$$\frac{\int d\lambda L^{\rm abs}_{\lambda,{\rm V}}}{N_{\rm V}\pi a^2_{\rm Grain} 4\pi} = \int d\lambda Q^{\rm abs}_\lambda B_\lambda(T_{\rm Grain}). \tag{11}$$

Because the temperature $T_{\rm Grain}$ cannot be separated from Eq. 11 without knowledge of the radiation field, an iterative approach is usually applied. To decrease the runtime of our program, we pre-calculate the integral $\int d\lambda Q^{\rm abs}_\lambda B_\lambda(T_{\rm Grain})$ for the expected temperature range ($T_{\rm Grain}$ = 0. . .2000 K, $\Delta T_{\rm Grain} = 0.1$ K). To derive $T_{\rm Grain}$, we compare these pre-calculated values with the left side of the integral.

In the case of additional heating (e.g., viscous heating in an active accretion disk or compressional heating during the collapse of a molecular cloud core), the right side of the equation of energy conservation has to be expanded by

$$L^{\rm add} = \int d\lambda \pi a^2_{\rm Grain} 4\pi Q^{\rm abs}(\lambda, a_{\rm Grain}) B_\lambda(T^{\rm add}_{\rm Grain}) \tag{12}$$

whereby $T^{\rm add}_{\rm Grain}$ is the dust grain temperature due to additional heating and $L^{\rm add}$ is the resulting luminosity. If the SED of the star (strongly) differs from that of a black body, $B_\lambda(T_{\rm eff})$ may be replaced by the relevant SED. Therefore, *any* heating source producing radiation in the near ultraviolet (NUV) . . . far infrared (FIR) wavelength range can be considered.

2.3. Algorithm

The radiative transfer problem is solved iteratively in our code:

1st Step: The model space has to be divided into ESCs. In each of these cells, the total energy of the radiation field being absorbed in its volume is stored. Based on this value, the dust grain temperature $T_{\rm Grain}$ (see Eq. 11) and the SED of the dust re-emission (see Eq. 9) in this cell will be calculated.

Because of the limited computer storage and therefore the limited number of ESCs, we apply the following criteria for an optimal splitting of the model space:

1. All symmetries of a given model should be taken into account (see Sect. 3.2, 3.3).
2. The partition of ESCs has to be coupled with the spatial distribution of the optical depth. Because the energy absorption gradient and, therefore, the dust temperature increases with increasing optical depth, the size of ESCs should decrease in optically thick regions.
3. Because of the geometrical dilution of the stellar radiation field, the absorption probability and therefore the temperature gradient strongly increases towards the radiation source. Hence, the ESC volume should decrease towards the star(s) even in the case of optically thin dust shells.

One has always to take into account that the increase of the resolution of the spatial dust temperature distribution due to an increase of the number of ESCs decreases the extinction probability of the test photons in a particular cell. Because of the large number of scattering and therefore absorption events which are needed to obtain the SED of the dusty medium with a low statistical noise, the simulation runtime increases.

According to the smallest characteristic length of all ESCs ($l_{\rm ESC_{min}}$), we define an upper ($\Delta l_{i_{\rm max}}$) and a lower limiting value ($\Delta l_{i_{\rm max}}$) for the stepwidth Δl_i of the test photon transfer to speed up the calculation of the sum in Eq. 5 (see Sect. 2.1). We choose $\Delta l_i = \Delta l_{i_{\rm max}}$ for the fast numerical integration of the optical depth along the actual path of the photon, and smoothly decrease Δl_i, if the difference $|\tau_{\rm ext} - \tilde{\tau}_{\rm ext}|$ becomes small (see Sect. 2.1, Eq. 4,5, and 6). If $\Delta l_i = \Delta l_{i_{\rm min}}$ or ϵ_τ is reached, the photon particle interaction takes place (typical values: $\Delta l_{i_{\rm max}} = 0.2\, l_{\rm ESC_{min}}$, $\Delta l_{i_{\rm min}} = 0.02\, l_{\rm ESC_{min}}$).

Furthermore, because the test-photon transfer is not coupled to the grid (resp. the distribution of ESCs), the numerical ESC

managment has to be highly optimized in respect to a fast assignment of the amount of absorbed energy to the according cell.

2nd Step: The radiation coming from the star(s) heats the dust due to absorption (total absorbed flux in the ESC #i: $\int d\lambda L^{\rm abs,star}_{\lambda,{\rm V_i}}$). The initial temperature of each ESC can be derived from Eq. 11, whereby

$$\int d\lambda L^{\rm abs}_{\lambda,{\rm V}} = \int d\lambda L^{\rm abs,star}_{\lambda,{\rm V_i}} \tag{13}$$

3rd Step: The dust re-emission will be simulated for all ESCs separately. The additionally absorbed flux in the ESC #i is $\int d\lambda L^{\rm abs,dust}_{\lambda,{\rm V_i}}$. The new dust temperatures can be derived from Eq. 11, whereby

$$\int d\lambda L^{\rm abs}_{\lambda,{\rm V}} = \int d\lambda L^{\rm abs,star}_{\lambda,{\rm V_i}} + \int d\lambda L^{\rm abs,dust}_{\lambda,{\rm V_i}} \tag{14}$$

4th Step: If one of the following two relations is *not* satisfied, the third step has to be repeated:

1. $\max(\Delta T(i) < T_{\rm max})$,
   where $\Delta T(i)$ is the change of the temperature in the ESC #i due to the dust re-emission (Step 3) and $T_{\rm max}$ is a given limit ($T_{\rm max} \approx$ a few Kelvin)
2. $\frac{|\int d\lambda L^{\rm e}_{\lambda,{\rm star}} - \int d\lambda L^{\rm obs}_{\lambda,{\rm star}} - \int d\lambda L^{\rm obs}_{\lambda,{\rm dust}}|}{\int d\lambda L^{\rm e}_{\lambda,{\rm star}}} < u_{\rm max}$,
   where $u_{\rm max}$ is a given value (we used $u_{\rm max} = 10^{-3} \ldots 10^{-5}$). $\int d\lambda L^{\rm obs}_{\lambda,{\rm star}}$ and $\int d\lambda L^{\rm obs}_{\lambda,{\rm dust}}$ are the luminosity of the star or the dust shell outside the model space, respectively.

In the case of additional heating sources Eq. 13 and 14 have to be modified accordingly.

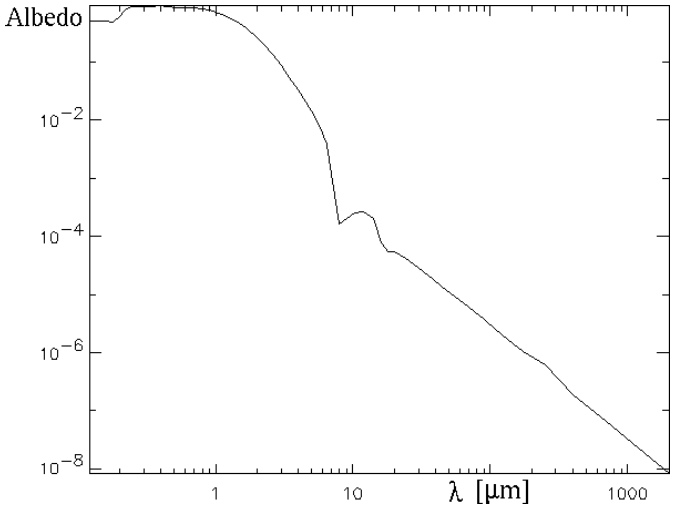

Fig. 2. Albedo of the dust grains, which has been used in our simulations in the considered wavelength range (λ=0.12 ... 2000 μm): spherical grains, consisting of astronomical silicate; radius: $a_{\rm Grain} = 0.12\,\mu$m, optical data from Draine & Lee 1984

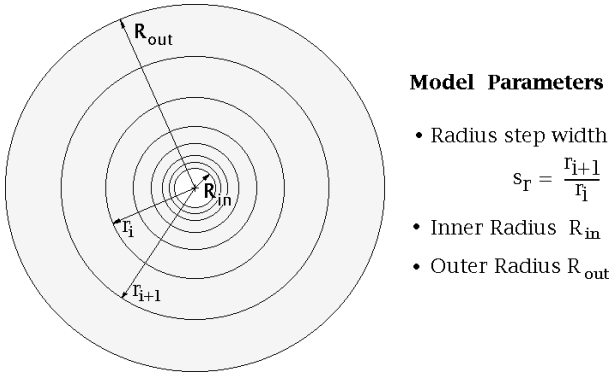

Fig. 3. 1D test model. The model space is subdivided into spherical dust shells with radii distributed equidistanly on a logarithmic scale. Each spherical shell symbolizes an ESC. The point-like star is located in the centre.

3. Tests

3.1. General model parameters

Because we have no special astrophysical object with individual features in mind to test the code, the number of model parameters was chosen to be as low as possible: All test models consist of a point-like star ($R_* = 10^9$m, $T_{\rm eff} = 5000$ K, black-body emission) embedded in a dust shell. The dust grains are spherical and consist of astronomical silicate ($a_{\rm Grain} = 0.12\,\mu$m, optical data from Draine & Lee 1984). The radiative transfer is simulated for 61 wavelengths being distributed nearly equidistantly on a logarithmic scale in the range of 0.12 ... 2000 μm. The albedo in this wavelength range of the considered dust grains is shown in Fig. 2.

3.2. 1D tests

The radiative transfer, always being handled three-dimensional in our code, is not coupled to the grid on which the energy storage cells and - depending on the model - the density distribution of the scattering medium is defined. Therefore, the radiative transfer can be fully tested on the basis of 1D models already. Because of the low computation time, compared with two- or three-dimensional models, this is of great importance. Beyond this, the comparison with 2D and 3D models is needed primarily because of numerical aspects (see Sect. 3.3, 3.4).

The model consists of a star in the centre of a spherical dust shell (inner radius $R_{\rm in} = 10$ AU, outer radius $R_{\rm out} = 10^3$ AU, dust density profile $n(r)$; see Fig. 3). The model space is subdivided into 50 spherical shells with radii distributed equidistantly on a logarithmic scale characterized by the *radius step width* $s_{\rm r} = r_{i+1}/r_i$ (we use $s_{\rm r} = 1.01 \ldots 1.2$). The inner radius of the innermost shell $R_{\rm in}$ symbolizes the dust grain sublimation radius. While $R_{\rm in}$ is predefined in our test calculations, it can be obtained self-consistently from the radiative transfer simulations itself.

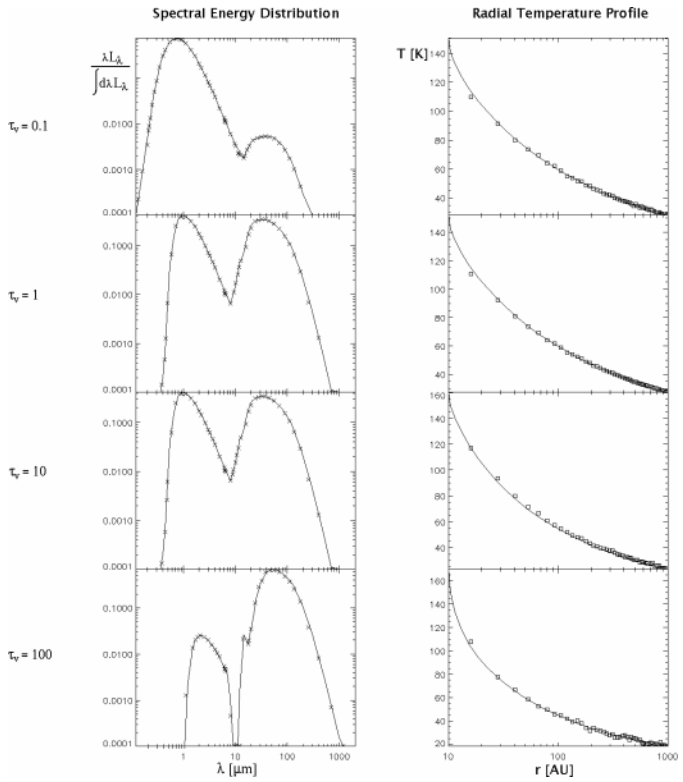

Fig. 4. SED and radial temperature profile for the 1D test case for 4 optical depths of the shell: $\tau_{\rm V}$ = 0.1, 1, 10, and 100 (see Sect. 3.2). $\tau_{\rm V}$ is the optical depth at λ=550 nm. Density profile: $n(r) = const.$ Crosses/open boxes: Simulation results of our code; Solid lines: Results obtained with the code of Chini et al. (1986)

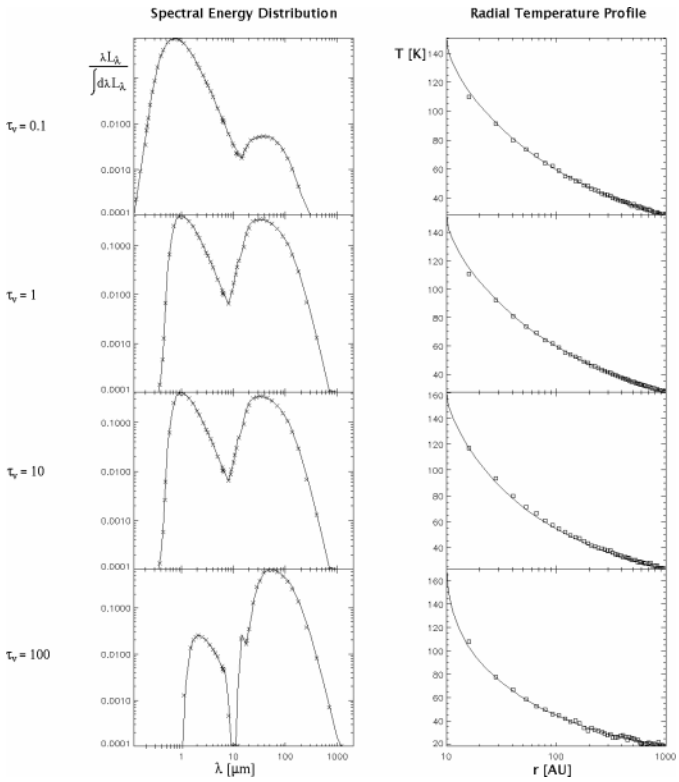

Fig. 5. SED and radial temperature profile for the 1D test case for 4 optical depths of the shell: $\tau_{\rm V}$ = 0.1, 1, 10, and 100 (see Sect. 3.2). $\tau_{\rm V}$ is the optical depth at λ=550 nm. Density profile: $n(r) \propto r^{-1}$ Crosses/open boxes: Simulation results of our code; Solid lines: Results obtained with the code of Chini et al. (1986)

In Fig. 4 the SED and the radial temperature profile are shown for a shell with a constant dust density, while Fig. 5 shows the results for a density profile following $n \propto r^{-1}$. In both cases, we considered the radiative transfer for the optical depths $\tau_{\rm V}$ = 0.1, 1, 10, and 100, where $\tau_{\rm V}$ is the optical depth at λ=550 nm. For comparison, the results obtained with the radiative transfer code of Chini et al. (1986) are shown. The differences between the results of the two codes are negligible even in the case of a high optical depth ($\tau_{\rm V}$=100). These results have also been compared with those calculated with the code of Menshchikov & Henning (1997; see also the test case calculations by Ivezic et al. 1997). We found the same good agreement between the results.

3.3. 2D tests

We considered two different 2D models of circumstellar disks: Fig. 6[A] shows the first model (Disk parameters: $n(r) \propto r^{-1}$, silicate grains, inner radius: 14 AU, outer radius: 10^3 AU, opening angle: $2\xi = 90^{\rm o}$, $\tau_{\rm V} = 5$; stellar parameters: $R_* = 10^9$ m, $T_{\rm eff} = 5000$ K). The model space is a sphere with the polar cones removed. The original sphere is subdivided into spherical shells with radii equidistantly distributed on a logarithmic scale (r_{i+1}/r_i=1.1). For the comparison, we used the code of Manske et al. (1998) which is an accelerated version of the code of Menshchikov & Henning (1997). This code solves the radiative transfer equation on a grid, whereby the grid points are distributed similar to the radii of the spherical shells in our code. In Fig. 7, the SED for two inclinations of the disk are shown: nearly edge-on and nearly face-on. Both codes produce the same reddening of the stellar radiation as well as the increase of the intensity of the re-emitted dust radiation in the edge-on case compared with the face-on case.

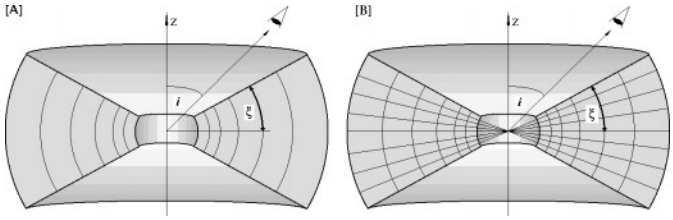

Fig. 6. 2D test model: Circumstellar disk. In both cases the model space is a sphere with the polar cones removed. The quantity i is the inclination of the disk with respect to the observer. The angle ξ is the half opening angle of the disk. **[A]** The ESCs are parts of spherical shells with radii distributed equidistantly on a logarithmic scale. For comparison of the radiative transfer results, we use the code of Manske et al. (1998). **[B]** Additionally, the model space is subdivided linearly in azimuthal direction. For comparison of the radiative transfer results, we use the code of Efstathiou & Rowan-Robinson (1990).

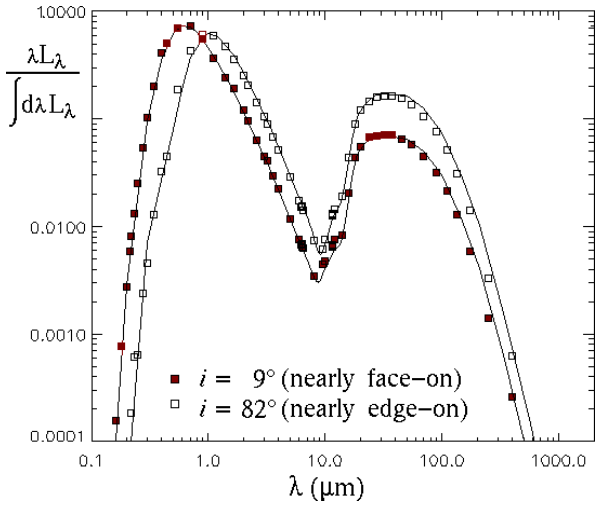

Fig. 7. SED for the 2D test configuration Fig. 6[B] seen under two different inclinations *i* of the disk. Our results (open and filled boxes) and those calculated with the code of Manske et al. (1998, solid lines) are shown.

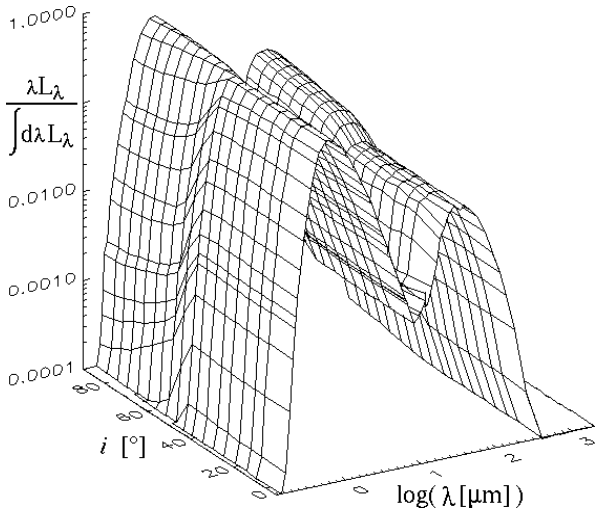

Fig. 8. SED of the 2D test configuration shown in Fig. 6 [B] as a function of the inclination *i* of the disk and wavelength λ. Opening angle of the disk: 2ξ=90°; Optical depth in the midplane (seen from the illuminating star): $\tau_{\rm V}$=5.04; $R_{\rm in} = 10\,{\rm AU}$, $R_{\rm out} = 400\,{\rm AU}$.

In the second model, the density distribution depends on the radial distance from the central star and the azimuthal angle Θ. Therefore, the model space is subdivided both in radial and azimuthal direction (see Fig. 6[B]). According to the density distribution defined by Efstathiou & Rowan-Robinson (1990, Eq. 17) we simulated the radiative transfer in this case for a density distribution following

$$R_{\rm in} \leq r \leq R_{\rm out} : n(r,\Theta) \propto r^{-1}\,(\frac{\pi}{2} - |\Theta|)^2 \tag{15}$$

$$\text{else}: \; n(r,\Theta) = 0 \tag{16}$$

where $R_{\rm out}$ is the outer radius of the disk and $R_{\rm in}$ is its inner radius. Fig. 8 shows the SED for different inclination angles of the disk for $R_{\rm in} = 10\,{\rm AU}$, $R_{\rm out} = 400\,{\rm AU}$, and $\tau_{\rm V}$=5.04. Furthermore, we considered the case of a constant dust density and compared our results with that of Efstathiou (1999, priv. communication). Their code solves the radiative transfer equation on a similar grid. We found an excellent agreement of the results.

Finally, we can conclude that the SEDs of both 2D models (Fig. 6[A] and [B]) obtained with our code show no significant differences to the results of the codes of Manske et al. (1998), Menshchikov & Henning (1998), and Efstathiou & Rowan-Robinson (1990).

3.4. 3D tests

In general, 3D models do not show any symmetries - in contrast to the 1D and 2D case, where the partition of the model space into ESCs is strongly adapted to its symmetry. Therefore, we use a cubical model space for 3D models (cartesian coordinates, side length $l_{\rm c}$). It is subdivided into smaller cubes (side length $0.5^{i_{\rm c}} l_{\rm c}$, $i_{\rm c} = 1, 2, \ldots$; see Fig. 9[B-1]) whereby their spatial size distribution is directly coupled to the spatial distribution of the optical thickness (examples see Fig. 9[B-2]. . .[B-4]). For this reason we define

$$\eta_{\rm V} = \sum_{i=1}^{j} C_{\rm ext_i} * \tilde{N}_{\rm V}(i), \tag{17}$$

where $\tilde{N}_{\rm V}(i)$ is the number of particles of the dust species $\#i$ in the volume V, $C_{\rm ext_i}$ is the corresponding extinction cross section, and j is the number of dust species. Firstly, $\eta_{\rm V}$ is determined in the entire model space (η_0). Afterwards, this cube is divided into 8 cubes with the half side length of the original cube. If the relation

$$\frac{\eta_{\rm V}(j)}{\eta_0} < \Psi, \tag{18}$$

where $\eta_{\rm V}(j)$ is the value of $\eta_{\rm V}$ in the "sub-cube" $\#j$ and Ψ is a user-defined value (usually $\Psi = 10^{-3\ldots5}$), is not satisfied, the considered "sub-cube" has to be divided once again, etc. . In Fig. 9[B-1]. . .[B-3] the result of this algorithm is shown for 3 different more or less complex dust configurations. The final cubes are the ESCs of the configuration.

Because of the lack of availability of another 3D model, we had to find another way for checking the code in three dimensions. This can be done with more symmetric configurations if these symmetries are not used. Here, we considered the radiative transfer in a spherical envelope with a constant dust density described in Sect. 3.2. The spatial discretization of the model space into ESCs is shown in Fig. 9[B-1]. The graphs in Fig. 10 show a good agreement between our results and those obtained with the 1D radiative transfer code of Chini et al. (1986). To demonstrate that the application of our code is mainly limited by the optical depth - both to high and to low optical depths - we chose a low test-photon number. If - on the one hand - the optical depth is too high ($\tau_\nu \gg 100$), the test photon transfer becomes very slow because of the increasing number of scattering events.

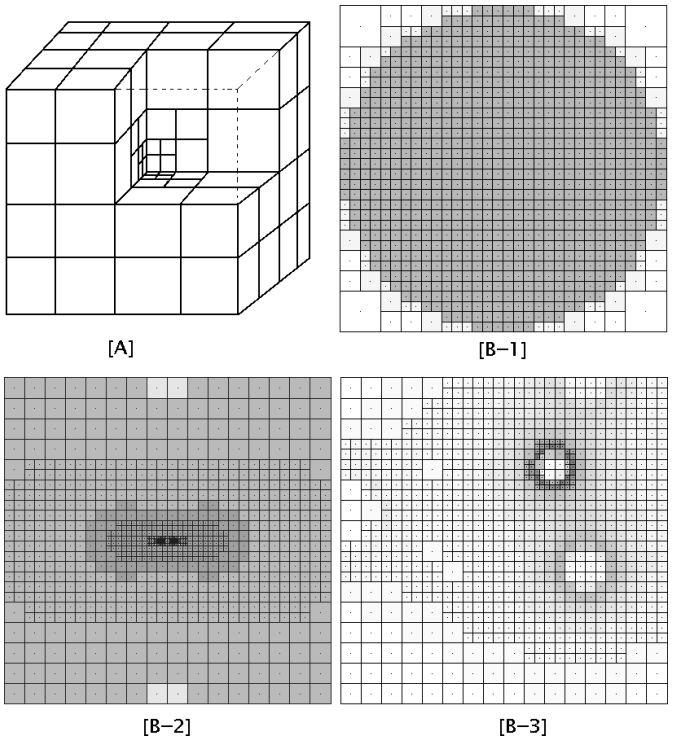

Fig. 9. [A] Example for the partition of the cubical model space into smaller cubical cells (ESCs) adapted to the optical depth distribution in the case of a 3D density distribution of the scattering medium; **[B]** Midplane of the spatial representation of the partition of the model space in the case of [B-1] a spherical density distribution ($n(r)$ = const.), [B-2] a Keplerian Disk (see Shakura & Sunyaev 1973), and [B-3] an arbitrary clumpy density distribution. Dark/bright fields symbolize high/low density regions. The dots mark the centre of each cell.

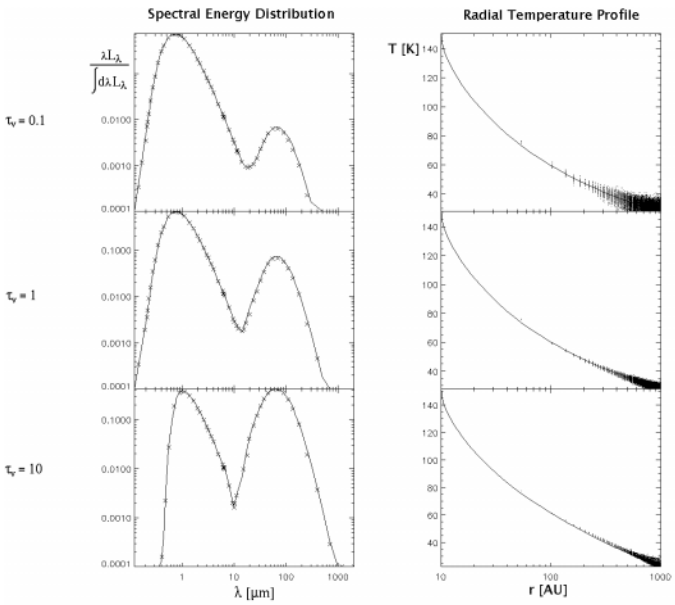

Fig. 10. SED and radial temperature profile for the 3D test case (see Sect. 3.4). Density profile: $n(r) = const.$ Crosses/open boxes: Simulation results of our code; Solid lines: Results obtained with the code of Chini et al. (1986)

The number of test photons has to be increased because of their exponentially decreasing mean path length which would lead to a considerable increase of the statistical noise of the temperature values in the outer regions. Furthermore, the number of iterations will increase because of the decreasing "numerical" thermal conduction. If - on the other hand - the optical depth is too low ($\tau_\nu \ll 0.01$), the decreased scattering probability and, therefore, the increased statistical noise of the dust temperature has to be compensated by increasing the number of test photons. In both (very low/high optical depth) cases the simulation runtime increases. To demonstrate the latter effect, the same test photon number was choosen for all 3D tests (τ_ν = 0.1, 1, and 10). Decreasing the optical depth, the statistical noise of the temperature in the outer ESCs of the shell increases (see Fig. 10).

4. Applications

4.1. Far-infrared radiative transfer in fragmented molecular cloud cores

As the first application of our code, we consider the radiative transfer in a fragmented molecular cloud core. The basis of our simulation is provided by a cloud collapse model which was simulated by Boss (1998) (Fig. N) with the three-dimensional gravitational radiative hydrodynamics code described in detail by Boss & Myhill (1992). The code calculates finite-difference solutions of the equations of hydrodynamics and gravitation for an inviscid, neutral gas including radiative transfer in the Eddington approximation. It is written in spherical coordinates (r, Θ, Φ), and solutions are obtained within a spherical volume. For this reason, we also used a spherical model space and described the density and ESC distribution by spherical coordinates. The grid points of the hydrodynamical model are defined to be the midpoints of the ESCs. The density and temperature at a certain grid point symbolizes the constant values in the whole ESC.

The radial grid resolution is $N_r = 51$ (including the central grid cell). It is defined in order to resolve the central region. The Θ-grid has $N_\Theta = 23$ for $\pi/2 \geq \Theta \geq 0$ with strongly concentrated grid points around the equatorial plane in order to resolve the midplane of the collapsing, rotating cloud. The Φ-grid is uniformly spaced with $N_\Phi = 64$. Therefore, our model consists of 137700 ESCs. The density in the midplane (perpendicular to the rotational axis) of the cloud is shown in Fig. 11[A]. The binary structure results from a Gaussian cloud with an initial density pertubation (Boss 1991, 1993; Klapp et al. 1993; Burkert & Bodenheimer 1996; Truelove et al. 1998), where the initial Gaussian radial density profile $\rho_i(r)$ is given a 10% non-axisymmetric pertubation of the form

$$\rho_i(r, \Phi) = \rho_i(r)[1 + 0.1\cos(2\Phi)] \tag{19}$$

The midplane temperature profile in the central region, resulting from a non-isothermal collapse, is shown in Fig. 11[B].

In our simulations, we used the same silicate grains as for the test of the code (see Sect. 3.1). The gas-to-dust mass ratio was assumed to be 100:1, whereby we used a dust grain density of $3.6\,\mathrm{g\,cm^{-3}}$.

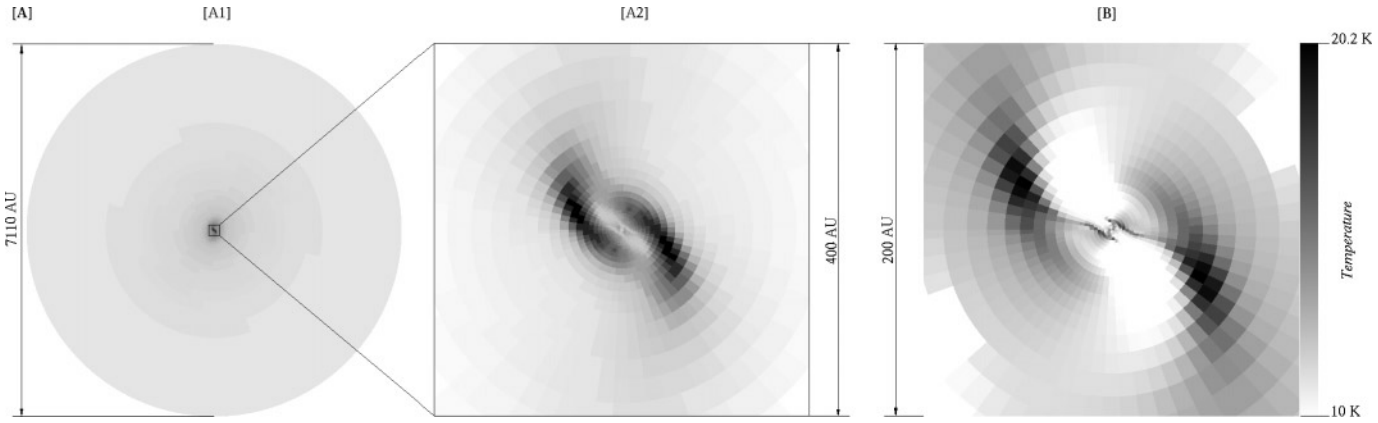

Fig. 11. [A] Midplane density structure of the collapsing cloud: [A1] whole configuration (diameter: 7110 AU), [A2] inner region (diameter: 400 AU). **[B]** Midplane temperature structure of the inner region of the cloud (radius: 200 AU)

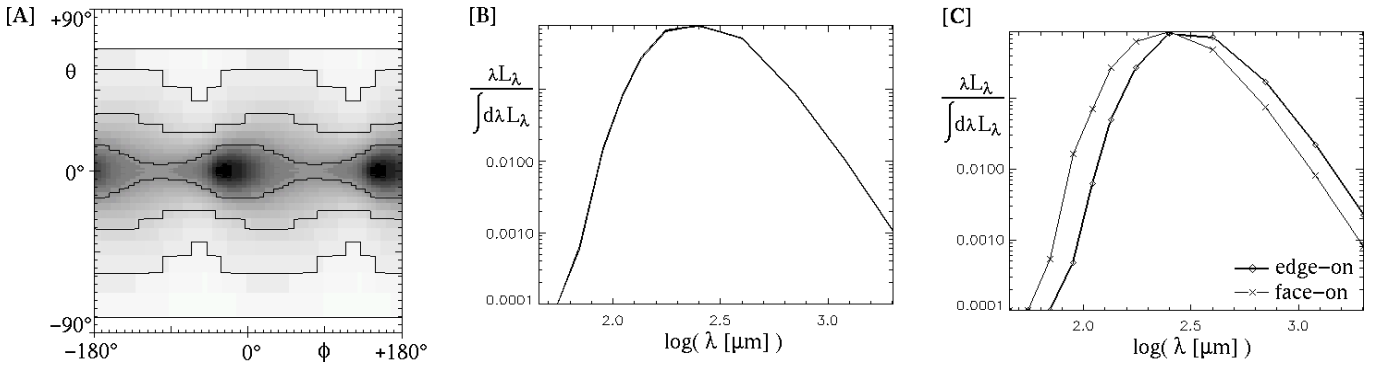

Fig. 12. [A] Optical depth $\tau(\lambda = 90\,\mu\mathrm{m})$ seen from the center as a function of the viewing direction decribed by Θ and Φ. The contour lines mark the optical depths of 4.56, 12.4, 28.0, and 61.1. Max. optical depth in the midplane: ≈ 68. Optical depth perpendicular to the midplane: 0.66. **[B]** SED of the entire system. There is no dependence of the SED on the inclination angle. **[C]** SED of the central region (radius: 203 AU). In the edge-on case, the SED shows a shift towards longer wavelengths compared with the face-on case (for explanation see Sect. 4.1).

Firstly, we calculated the SED. It was found that there is no dependence of the SED on the inclination angle despite the optical depth in the midplane being much higher (factor $\approx 10^2$) than perpendicular to it (see Fig. 12[A], 12[B]). This can be explained by the small extent of the emitting region in connection with scattering processes in the much larger shell which smeares out the inclination dependence. For this reason, we additionally determined the SED of a central spherical volume with only a tenth of the diameter of the whole configuration. In this case, the dependence of the SED on the inclination angle is clearly seen in Fig. 12[C]. The SED obtained in the edge-on case is reddened compared to the SED of the face-on case. This can be explained by the low dust grain temperature (T_{Grain}=10...20.2 K). The largest amount of radiation is therefore emitted at long wavelengths ($\frac{\lambda S_\lambda}{\int d\lambda S_\lambda}$ has its maximum at $\lambda \approx 250\,\mu$m) where the configuration has a low optical thickness even in the edge-on case.

Secondly, we calculated the intensity and polarization maps for different inclination angles and two wavelengths ($\lambda = 90\,\mu$m, $400\,\mu$m; see Fig. 13). Only in the case of the edge-on orientation, the intensity maps are different: While the midplane is optically thin at $\lambda = 400\,\mu$m and the intensity reaches its maximum in the midplane (where the temperature has its maximum), the midplane is optically thick at $\lambda = 90\,\mu$m, where the intensity has therefore maxima below and above the midplane (see also Sect. 4.2).

The polarization angle approximately follows the iso-density curves and, therefore, the iso-intensity curves. The polarization degree has a local minimum in the two centers of emission. It reaches its maximum already in the high-density inner region and strongly decreases with increasing distance from the centre. The polarization degree is extremly low for both wavelengths and practically not detectable ($\approx 10^{-4} \ldots 10^{-6}$ %). This can be explained by the low albedo of the scattering dust grains (1.9×10^{-7}) which leads to a negligible intensity of the scattered photons compared to that of unscattered photons. From this follows, that the total flux is dominated by the non-scattered and therefore unpolarized photons arising from the outer optically thin regions, and the total polarization becomes very low. The described strong decrease of polarization with decreasing density and increasing distance from the centers of emission can be explained the same way. In contrast to this result, the observed polarization degrees of molecular clouds have values of a few percent which can only be produced by aligned grains (e.g., Dowell 1997, Novak et al. 1997, Hildebrand et al. 1993,

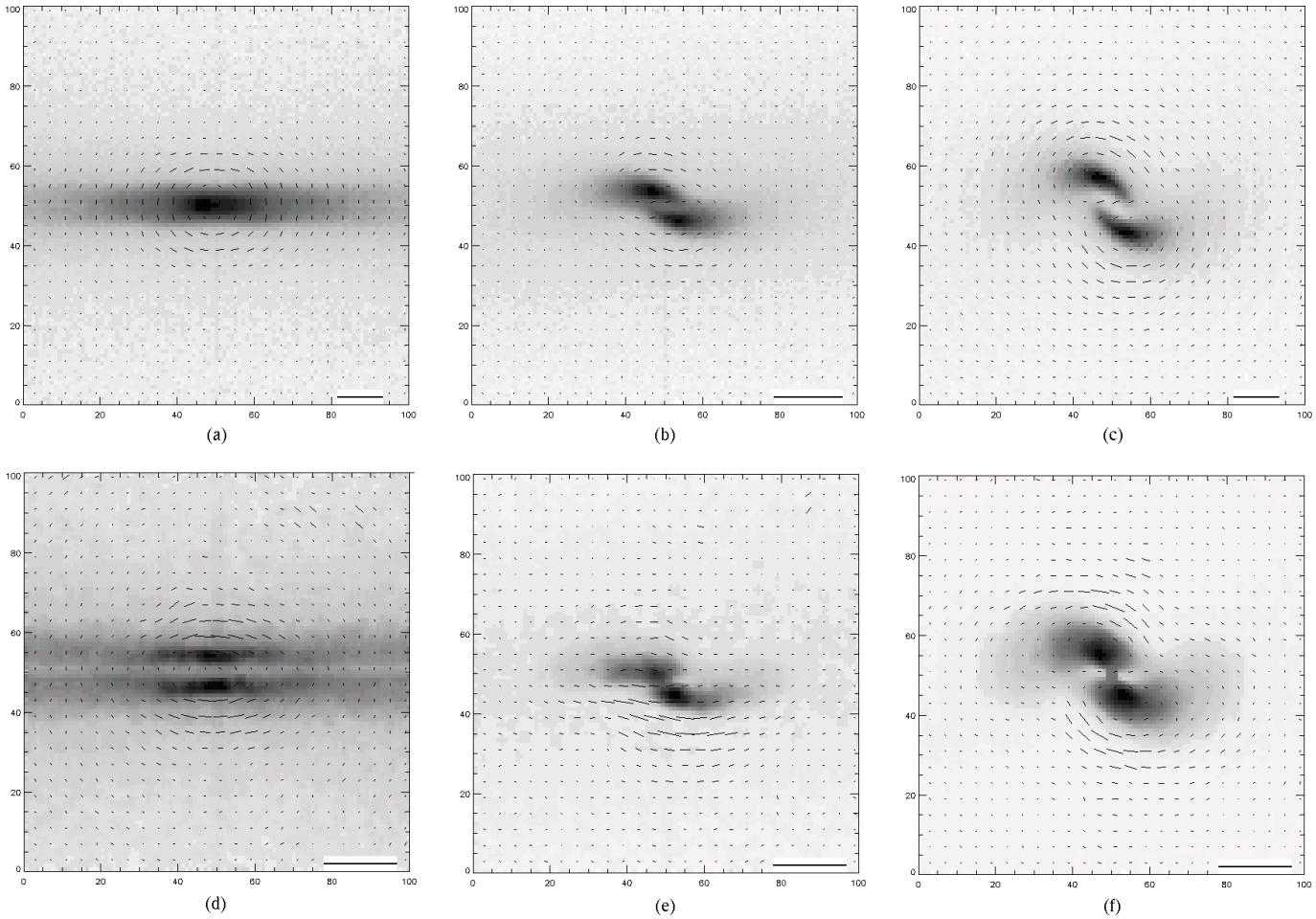

Fig. 13a–f. Intensity maps with overlayed polarization structures of the fragmented molecular cloud core. **a–c**: $\lambda = 400\,\mu$m. **d–f**: $\lambda = 90\,\mu$m. Diameter of the projected region: 237 AU. The vertical line in the upper right edge of each map symbolizes the polarization degree of $P_{\rm l} = 5.96 \times 10^{-6}$ % ($\lambda = 400\,\mu$m) resp. $P_{\rm l} = 3.81 \times 10^{-4}$ % ($\lambda = 90\,\mu$m). Inclination angles: **a**,**d** 90°; **b**,**e** 60°; **c**,**f** 0°.

Morris et al. 1992, Hildebrand et al. 1990, Gonatas et al. 1990). Then, in addition to the polarization due to scattering, dichroic extinction may play an important role as a source of polarization for radiation of long wavelengths (see e.g., Greaves et al. 1999, Efstathiou et al. 1997, Wood 1996, 1997, Larson et al. 1996, Casali 1995, Hildebrand & Dragovan 1995 Whittet et al. 1994). This issue will be investigated in a future paper.

4.2. Radiative transfer in a protostellar disk

We investigated the radiative transfer in a protostellar disk of $M = 1.14\,{\rm M}_\odot$. We used the spatial density and temperature distribution obtained by Yorke (1999, priv. communication). The hydrodynamic code solves the standard equations of hydrodynamics with radiation transport and the Poisson equation for the gravitational potential (Black & Bodenheimer 1975). The two-dimensional hydrodynamic code of Ròżyczka (1985) with second-order accurate advection is employed. Shocks are treated by including artificial viscosity. Physical viscosity is not included and angular momentum transport during the collapse is assumed to be negligible. The midplane density distribution is presented in Fig. 14[A],[C]. Because of the axisymmetry of the configuration, we use the same subdivision of the model space as for the comparison with the results of Efstathiou (1999, priv. communication) (see Sect. 3.3; Fig. 6[B]; Efstathiou & Rowan-Robinson 1990). In particular, the opening angle of the disk is set to π (full sphere), the number of radial grid points is 50 (distributed equidistantly on a logarithmical scale, whereby r_{i+1}/r_i = 1.05), and the model is divided into 36 equidistantly spaced intervalls in azimuthal direction. The grid points mark the center of the corresponding ESCs. The density and temperature is constant inside each ESC and equal to that of the corresponding grid point.

We used the same dust grain parameters as for the radiative transfer in the fragmented molecular cloud core (see Sect. 4.1).

In Fig. 15, the SED of the entire system is shown for two different inclinations of the disk. In the edge-on orientation, the SED is strongly increasing with wavelength and the IR/NIR radiation of the covered inner parts is weakened (for comparison see Menshchikov & Henning 1997, Sonnhalter et al. 1995). In the face-on orientation the SED shows a significant 9.7 μm

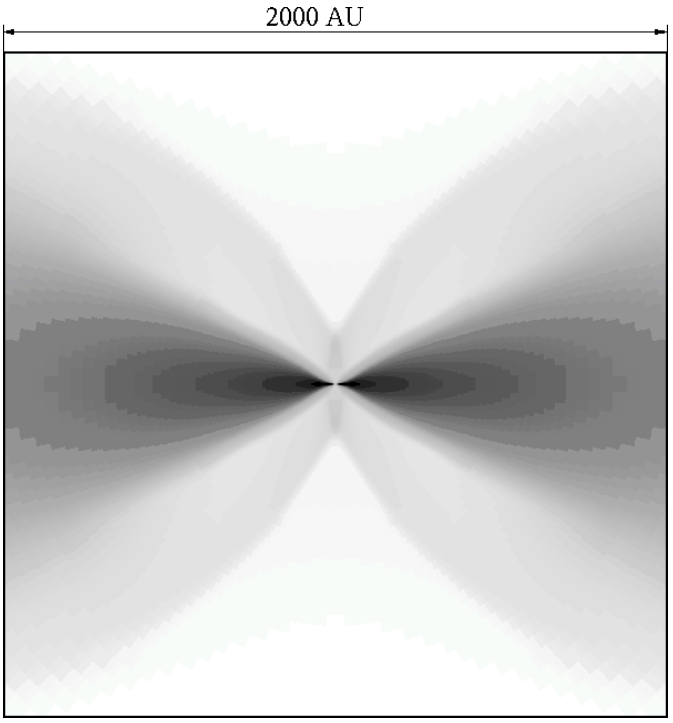

Fig. 14. Density structure of protostellar disk perpendicular to the midplane. (for comparison: radius of the entire disk = 3500 AU). The maximum temperature amounts to 532 K.

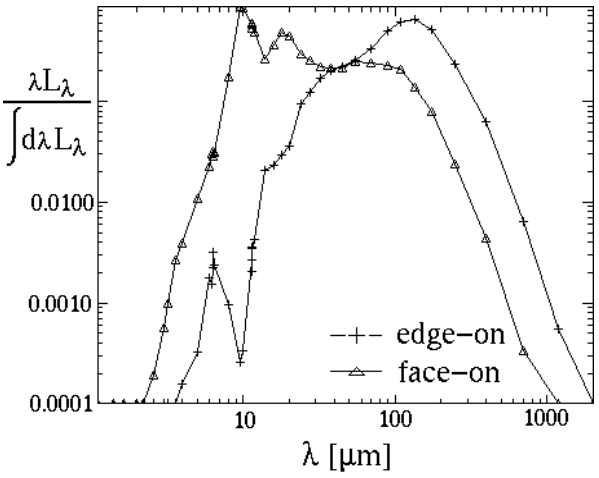

Fig. 15. SED of the entire system (radiation of the warm dust, no central star). Edge-on orientation: 9.7 μm silicate absorption band; Face-on orientation: relatively flat SED at MIR wavelengths, 9.7 μm silicate emission band

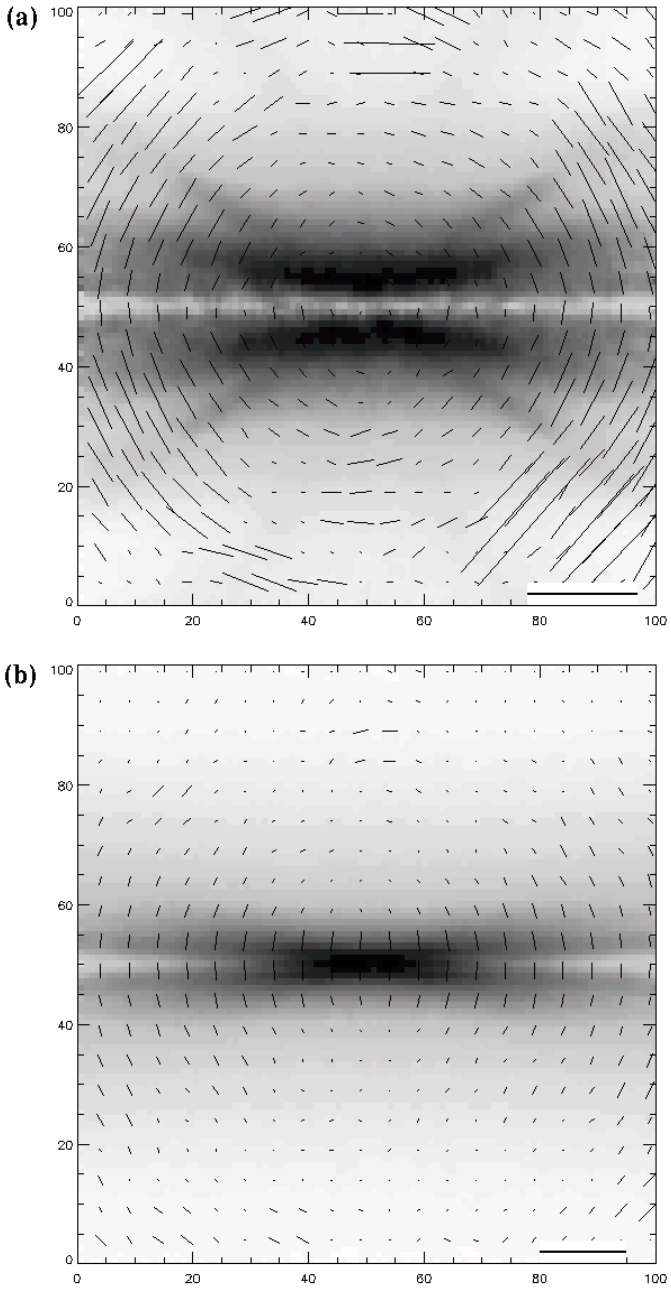

Fig. 16a and b. Intensity maps with overlayed polarization structures of the disk seen edge-on. **a** $\lambda = 90\,\mu$m, **b** $\lambda = 400\,\mu$m. The horizontal line in the upper right edge of each map symbolizes the polarization degree **a** $P_{\rm l} = 1.91 \times 10^{-4}\,\%$ resp. **b** $P_{\rm l} = 2.98 \times 10^{-6}\,\%$.

silicate emission band, while the silicate dust produces an absorption band in the edge-on orientation.

Intensity maps with overlayed polarization structures at different inclinations of the disk are shown in Fig. 16 for $\lambda = 90\,\mu$m and $400\,\mu$m. For $\lambda = 90\,\mu$m, the midplane is optically thick ($\tau(\lambda$=90 μm)=78.1). The intensity reaches its maximum below and above the midplane. This intensity map is similar to that of HH30 (e.g., in the K-band; see e.g. Burrows et al. 1996, Wood et al. 1998). In contrast to this, the midplane is optically thin at $\lambda = 400\,\mu$m and the intensity maximum is located in the midplane.

Because of the low albedo of the dust grains in the mid/far infrared wavelength range, the polarization is very low at both wavelengths ($P_{\rm l,\,max}(\lambda = 90\,\mu{\rm m}) \approx 10^{-4}\,\%$, $P_{\rm l,\,max}(\lambda = 400\,\mu{\rm m}) \approx 10^{-6}\,\%$) and will not be detectable. In the case of $\lambda = 400\,\mu$m, the regions of "large" polarization degrees are more concentrated to the midplane.

Finally, we investigated the SED of the system with an additional heating star in the center ($L = 2\,L_\odot$, $T = 6000\,$K;

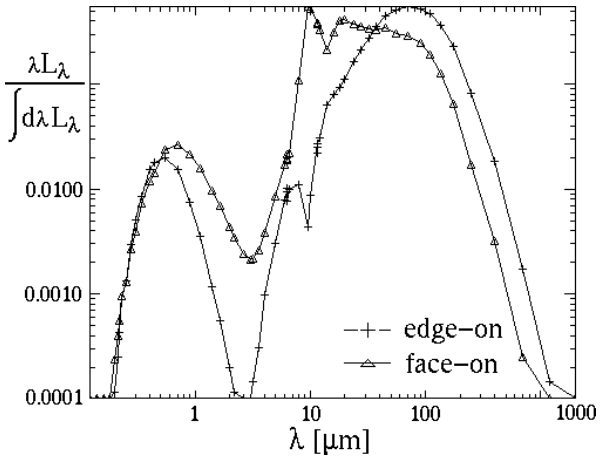

Fig. 17. SED of the disk with an additional star in the centre. Stellar parameters: $L = 2\,\mathrm{L}_\odot$, $T = 6000\,\mathrm{K}$.

see Fig. 17) Such a configuration has been calculated because in a further evolution of the system the formation of a pre-main sequence star in the centre of the configuration can be expected. We found that the percentage of short wavelenght stellar radiation is high even in the edge-on case. This can be explained by light scattering in the optically thin lobes perpendicular to the midplane.

5. Conclusions

We described the first code for three-dimensional self-consistent continuum radiative transfer calculations. It is based on an efficient implementation of the Monte-Carlo method. Apart from the simulation of SEDs, image maps, the spatial temperature distributions of arbitrary dust density configurations with embedded stars or similar energy sources (e.g., active accretion disks around young stellar objects), and polarization maps of those systems can be computed.

We succesfully tested the new code by extensive comparisons with the results of other well-tested radiative transfer codes (Chini et al. 1986; Efstathiou & Rowan-Robinson 1990,1995; Menshchikov & Henning 1997; Ivezic et al. 1997; Manske et al. 1998). We should stress that such tests are absolutely necessary in the case of multidimensional radiative transfer computations. The code works most efficiently in the range of optical depths between 0.01 and 100.

To demonstrate the power of the new technique, we applied the code to the radiative transfer in two density configurations being the result of hydrodynamical computations of Boss (1998) and Yorke (1999, priv. communication). We simulated the SEDs, intensity and polarization maps of a fragmented molecular cloud core and a protostellar disk with and without a central stellar radiation source.

We found that in the case of a young molecular cloud core the SED does not depend on the inclination angle because of the obscuration effect of the massive envelope. The SED becomes sensitive to the inclination angle when the envelope is removed (or accreted). The polarization produced by scattering alone is practically unobservable at wavelengths longer than 90 μm. In the case of the disk system a strong dependence of the SED on the inclination angle has been found. This confirms earlier results obtained by Sonnhalter et al. (1995) and Menshchikov & Henning (1997). The intensity maps at 90 and 400 μm show very distinct differences because of optical depth effects. Polarization at long wavelengths due to scattering would again not be observable.

In the future, we will apply this code to a wide range of radiative transfer problems, e.g., the radiative transfer in the clumpy environment of YSOs and AGNs, in young binary systems with circumstellar disks, and circumstellar disks with embedded proto-planets.

In respect to the future development of this code we direct our attention to the implementation of light scattering by aligned dust grains. In this respect it is our aim to investigate the connections between the occurence and orientation of spheroidal dust particles, magnetic fields, and polarization in young stellar objects, the interstellar medium and AGNs.

Acknowledgements. We thank A. Efstathiou and R. Chini for providing their 1D/2D radiative transfer codes or the results for comparison with the results of our code. We thank O. Fischer, A.B. Menshchikov, and V. Manske for many discussions about radiative transfer. Furthermore, we thank H. W. Yorke and A. P. Boss for providing the spatial density and temperature distribution of a protostellar disk and a fragmented molecular cloud core.

This research was supported by the DFG grant Ste 605/10 within the programme “Physics of star formation”.

Appendix A: concept of the programme

Our code consists of 4 decoupled parts:

1. Radiative transfer routines and data input/output managment
2. Description of the radiative behaviour of the stars or other “primary” radiation sources (SED, spatial extent, isotropic/anisotropic radiation)
3. Definition of the spatial density distribution of scatterers (dust grains, electrons): may be defined on a grid or given analytically
4. Definition of the grid for absorption and re-emission (1D, 2D, and 3D grids; different implementations)

While the first part of our program is fixed, part 2. . .4 are always adapted to a special model. In particular, the fourth part is very decisive for both the runtime of the code and the accuracy of the results.

Appendix B: scattering matrices

The scattering matrix (special Mueller Matrix) for the description of the modification of the Stokes vector due to the interaction of a photon with a spherical, homogeneous dust particle

(*Mie scattering*) is

$$\hat{S(\theta)} = \begin{pmatrix} S_{11}(\theta) & S_{12}(\theta) & 0 & 0 \\ S_{12}(\theta) & S_{11}(\theta) & 0 & 0 \\ 0 & 0 & S_{33}(\theta) & S_{34}(\theta) \\ 0 & 0 & -S_{34}(\theta) & S_{33}(\theta) \end{pmatrix} \tag{B1}$$

with

$$\begin{aligned} S_{11}(\theta) &= \tfrac{1}{2}(|S_1(\theta)|^2 + |S_2(\theta)|^2 + |S_3(\theta)|^2 + |S_4(\theta)|^2) \\ S_{12}(\theta) &= \tfrac{1}{2}(|S_2(\theta)|^2 - |S_1(\theta)|^2 + |S_4(\theta)|^2 - |S_3(\theta)|^2) \\ S_{33}(\theta) &= \mathrm{Re}\{S_1(\theta)S_2^*(\theta) + S_3(\theta)S_4^*(\theta)\} \\ S_{34}(\theta) &= \mathrm{Re}\{S_2(\theta)S_1^*(\theta) + S_4(\theta)S_3^*(\theta)\} \end{aligned} \tag{B2}$$

$$\begin{aligned} S_1 &= \textstyle\sum_{n=1}^{\infty} \frac{2n+1}{n(n+1)}(a_n\pi_n + b_n\tau_n) \\ S_2 &= \textstyle\sum_{n=1}^{\infty} \frac{2n+1}{n(n+1)}(b_n\pi_n + a_n\tau_n) \\ S_3 &= S_4 = 0 \end{aligned} \tag{B3}$$

$$\begin{aligned} a_n &= \frac{\psi_n'(mx)\psi_n(x) - m\psi_n(mx)\psi_n'(x)}{\psi_n'(mx)\zeta_n(x) - m\psi_n(mx)\zeta_n'(x)} \\ b_n &= \frac{m\psi_n'(mx)\psi_n(x) - \psi_n(mx)\psi_n'(x)}{m\psi_n'(mx)\zeta_n(x) - \psi_n(mx)\zeta_n'(x)} \end{aligned} \tag{B4}$$

$$\begin{aligned} \pi_n(\cos\theta) &= \tfrac{1}{\sin\theta} P_n^1(\cos\theta) \\ \tau_n(\cos\theta) &= \tfrac{d}{d\theta} P_n^1(\cos\theta) \end{aligned} \tag{B5}$$

where $P_n^1(\cos\theta)$ are Legendre polynomals, $\psi_n(x)$ and $\zeta_n(x)$ are Riccati-Bessel functions, m is the relative refractive index, and $x = \frac{2\pi a}{\lambda}$ is the scattering parameter.

In the case of *Thomson scattering* the - wavelength-independend - scattering matrix is

$$\begin{aligned} S_{11}(\theta) &= S_{22}(\theta) = \tfrac{1}{2}(cos^2(\theta) + 1) \\ S_{12}(\theta) &= S_{21}(\theta) = \tfrac{1}{2}(cos^2(\theta) - 1) \\ S_{33}(\theta) &= S_{44}(\theta) = cos(\theta) \\ S_{13} &= S_{31} = S_{23} = S_{32} = 0 \\ S_{14} &= S_{24} = S_{34} = S_{43} = 0 \end{aligned} \tag{B6}$$

References

Bianchi S., Ferrara A., Giovanardi C., 1996, ApJ 465, 127
Bickel W.S., Bailey W.M., 1985, Am. J. Phys. 53 (5), 468
Black D.C., Bodenheimer P., 1975, ApJ 199, 619
Bohren C.F., Huffman D.R., 1983, Absorption and scattering of light by small particles. John Wiley & Sons, New York
Boissé P., 1990, A&A 228, 483
Boss A.P., Yorke H.W., 1990, ApJ 353, 236
Boss A.P., 1991, Nature 351, 298
Boss A.P., Myhill E.A., 1992, ApJS 83, 311
Boss A.P., 1993, ApJ 410, 157
Boss A.P., 1998, ApJ 501, L77
Bouquet S., Tortel B., Burgan J.R., 1990, A&A, 231, 289
Burkert A., Bodenheimer P., 1996, MNRAS 280, 1190
Burrows C.J., Stapelfeldt K.R., Watson A.M., et al., 1996, ApJ 473, 437
Capetti A., Axon D.J., Macchetto F., Sparks W.B., Boksenberg A., 1995a, AJ 446, 155
Capetti A., Axon D.J., Macchetto F., Sparks W.B., Boksenberg A., 1995b, AJ 448, 600
Capetti A., Axon D.J., Macchetto F., Sparks W.B., Boksenberg A., 1995c, AJ 446, 155
Casali M.M., 1995, MNRAS 277, 1385
Chini R., Kruegel E., Kreysa E., 1986, A&A 167, 315
Colomb F.R., Pöppel W.G.L., Heiles C., 1980, A&AS 40, 47
Dent W.R.F., 1988, ApJ 325, 252
Dittmann O., 1995, PhD thesis
Dowell C.D., 1997, ApJ 487, 237
Draine B.T., Lee H.M., 1984, ApJ 285, 89
Efstathiou A., Rowan-Robinson M., 1990, MNRAS 245, 275
Efstathiou A., Rowan-Robinson M., 1995, MNRAS 273, 649
Efstathiou A., McCall A., Hough J.H., 1997, MNRAS 285, 102
Fischer O., Henning Th., Yorke H.W., 1994, A&A 284, 187
Gonatas D.P., Engargiola G.A., Hildebrand R.H. et al., 1990, ApJ 357, 132
Greaves J.S., Holland W.S., Minchin N.R., Murray A.G., Stevens J.A., 1999, A&A 344, 668
Henning Th., 1985, ApSS 114, 401
Hildebrand R.H., Gonatas D.P., Platt S.R. et al., 1990, ApJ 362, 114
Hildebrand R.H., Davidson J.A., Dotson J., Figer D.F., Novak G., Platt S.R., Tao L., 1993, ApJ 417, 565
Hildebrand R.H., Dragovan M., 1995, ApJ 450, 663
Ivezic Z., Groenewegen M.A.T., Menshchikov A., Szczerba R., 1997, MNRAS 291, 121
Kishimoto M., 1996, ApJ 468, 606
Klapp J., Sigalotti L.D.G., DeFelice F., 1993, A&A 273, 175
Knuth D.E., 1989, in "The art of scientific computing (FORTRAN version)", eds. Press W.H., Flannery B.P., Vetterling W.T., Cambridge University Press, Cambridge, p. 196–199
Larson K.A., Whittet D.C.B., Hough J.H., 1996, ApJ 472, 755
Leung C.M., 1975, ApJ 199, 340
Lopez B., Mekarnia D., Lefevre J., 1995, A&A 296, 752
Lorenz-Martins S., De Araujo F.X., 1998, MNRAS 291, 296
Macchetto F., Capetti A., Sparks W.B., Axon D.J., Boksenberg A., 1994, ApJ 435, L15
Manske V., Henning Th., 1998, A&A 337, 85
Manske V., Henning Th., Menshchikov A. B., 1998, A&A 331, 52
Menshchikov A.B., Henning Th., 1997, A&A 318, 879
Morris M., Davidson J.A., Werner M., Dotson J., Figer D.F., Hildebrand R., Novak G., Platt S., 1992, ApJ 399, L63
Novak G., Dotson J.L., Dowell C.D., Goldsmith P.F., Hildebrand R.H., Platt S.R., Schleuning D.A., 1997, ApJ 487, 320
Och S.R., Lucy L.B., Rosa M.R., 1998, A&A 336, 301
Pagani L., 1998, A&A 333, 269
Pier E.A., Krolik J.H., 1992, ApJ 401, 99
Rosen A., Bregman J.N., 1995, AJ 440, 634
Ròżyczka M., 1985, A&A 143, 59
Shakura N.I., Sunyaev R.A., 1973, A&A 24, 337
Sonnhalter C., Preibisch T., Yorke H.W., 1995, A&A, 299, 545
Spaans M., 1996, A&A 307, 271
Spagna G.F., Leung C.M., Egan M.P., 1991, ApJ 279, 232
Stenholm L., 1994, A&A 290, 393
Truelove J.K., Klein R.I., McKee C.F., Holliman J.H., Howell L.H., Greenough J.A., Woods D.T., 1998, ApJ 495, 821
Whitney B.A., Hartmann Lee, 1992, ApJ 395, 529
Whitney B.A., Hartmann Lee, 1993, ApJ 402, 605
Whittet D.C.B., Gerakines P.A., Carkner A.L., Hough J.H., Martin P.G., Prusti T., Kilkenny D., 1994, MNRAS 268, 1
Witt A.N., Gordon K.D., 1996, ApJ 463, 681
Wolf S., Fischer O., Pfau W., 1998, A&A 340, 103
Wood K., 1996, AAS 189, #67.08
Wood K., 1997, ApJ 477, L25
Wood K., Kenyon S.J., Whitney B., Turnbull M., 1998, ApJ 497, 404
Yorke H.W., 1980, A&A 86, 268
Yorke H.W., Bodenheimer P., Laughlin G., 1993, ApJ 411, 274